

Thermoelectric properties of bismuth-selenide films with controlled morphology and texture grown using pulsed laser deposition

Phuoc Huu Le^a, Chien-Neng Liao^b, Chih Wei Luo^{c,1}, Jiunn-Yuan Lin^d, Jihperng Leu^{a,*}

^a Department of Materials Science and Engineering, National Chiao Tung University, Hsinchu, 30049, Taiwan, ROC

^b Department of Materials Science and Engineering, National Tsing-Hua University, Hsinchu, 30013, Taiwan, ROC

^c Department of Electrophysics, National Chiao Tung University, Hsinchu, 300, Taiwan, ROC

^d Institute of Physics, National Chiao Tung University, Hsinchu, 300, Taiwan, ROC



ARTICLE INFO

Article history:

Received 24 June 2013

Received in revised form 31 July 2013

Accepted 14 August 2013

Available online 30 August 2013

Keywords:

Bi₂Se₃

Thermoelectric properties

Nanostructure morphologies

Pulsed laser deposition (PLD)

SiO₂/Si(1 1 1) substrates

ABSTRACT

Polycrystalline, thermoelectric thin films of bismuth selenide (Bi₂Se₃) were grown on SiO₂/Si (1 1 1) substrates, using pulsed laser deposition (PLD). Bi₂Se₃ films with highly *c*-axis-oriented and controlled textures were fabricated by maintaining the helium gas pressure (*P*) between 0.7 and 173 Pa and the substrate temperature (*T_s*) between 200 and 350 °C. The carrier concentration (*n*) of films decreased with increasing *P*, which was attributed to the increase of Se concentration from Se deficiency (*P* ≤ 6.7 Pa) to stoichiometry to slight Se enrichment (*P* ≥ 40 Pa). The Seebeck coefficient (*S*) was enhanced considerably because of the reduction in *n*, following the *S* ~ *n*^{-2/3} relation approximately. The average grain size increased from approximately 100 to 500 nm when *T_s* was raised from 200 to 350 °C, resulting in enhanced carrier mobility (*μ*) and electrical conductivity (*σ*) and a reduced full width at half maximum of (0 0 6) peaks. The shape of grains transformed from rice-like at *T_s* of 200–250 °C to layered-hexagonal platelets (L-HPs) or super-layered flakes (S-LFs) at *T_s* of 300–350 °C. Films that were grown at 300 °C and 40 Pa and contained highly *c*-axis oriented L-HPs possessed the highest power factor (PF = *S*²*σ*), which reached 5.54 μW cm⁻¹ K⁻², where *S* = 75.8 μV/K and *σ* = 963.8 S cm⁻¹.

© 2013 Elsevier B.V. All rights reserved.

1. Introduction

Thermoelectric (TE) materials are used in appliances such as heat pumps and power generators [1–3]. The effectiveness of a thermoelectric material is defined by the dimensionless thermoelectric figure of merit ZT = $\sigma S^2 T / \kappa$, where σ , S , κ , and T are the electrical conductivity, Seebeck coefficient, thermal conductivity, and absolute temperature, respectively [4,5]. The quantity σS^2 is commonly used to represent the thermoelectric power factor (PF). For enhancing ZT value, an increase in PF together with a decrease in thermal conductivity is required. However, the coupling among thermoelectric parameters limits the efficiency and the practical applications of a TE material [5,6]. For example, S and σ ($=ne\mu$) are coupled through the relationship between S and n , expressed by $|S| \sim n^{-2/3}$ for degenerate semiconductors [6], or by $|S| \sim (1+R)n^{-2/3}$ for semiconductors, where R is the scattering parameter [7].

The narrow-bandgap ($E_g \sim 0.3$ eV) semiconductor Bi₂Se₃ and other $A_2^{VI}B_3^{VI}$ -type compounds such as Bi₂Te₃ and Sb₂Te₃ are effective TE materials near room temperature [3,8]. A considerable amount of recent efforts to enhance TE performance has been devoted to the synthesis of Bi₂Se₃ nanostructures such as hexagonal flakes [9] and nanoflakes [10], using the solvo-thermal method and chemical bath deposition, respectively. However, few studies have reported the growth of Bi₂Se₃ thin films using pulsed laser deposition (PLD, a physical technique) or the characterization of the TE properties of such films. PLD is a versatile technique that controls deposition parameters and thereby enables films to be fabricated with multi-element stoichiometry as well as diverse structures and morphologies. Recent studies have revealed that the TE properties of Bi₂Te₃ films with distinct, controlled morphologies can be enhanced at certain ambient pressure (*P*) and substrate temperature (*T_s*) using PLD [11–13] or sputtering [14]. Bi₂Se₃ is more sensitive than Bi₂Te₃ to *T_s* because the vapor pressure of Se is higher ($P_{Se} > P_{Te} > P_{Bi}$ [15]), and therefore Bi₂Se₃ is often heavily *n*-type doped (because of the Se vacancy arising from Se evaporation) [16,17]. We postulated that the compositions and vacancies of the thin film can be controlled by changing *P*, and therefore we used Bi₂Se₃, which is considered a suitable candidate material for investigating the incompletely understood effects of *T_s* and *P* on properties of the films.

* Corresponding author. Tel.: +886 35131420; fax: +886 35724727.

E-mail addresses: cwluo@mail.nctu.edu.tw (C.W. Luo), jimleu@mail.nctu.edu.tw (J. Leu).

¹ Tel.: +886 35712121/56196.

In this work, we systematically investigate the effects of P and T_s on the structure and morphology of Bi_2Se_3 thin films. The in-plane electrical and TE properties of the films were characterized and an optimized processing window of P and T_s conditions was determined for enhancing the PF of Bi_2Se_3 . The coupling of S and n has been demonstrated. Our results provide a comprehensive understanding of optimal PLD conditions and morphology of Bi_2Se_3 thin films for TE applications.

2. Experimental details

Bi_2Se_3 thin films were deposited on SiO_2/Si (111) substrates at T_s of 200–350 °C and P of 0.7–173 Pa using PLD. UV pulses (15–20 ns duration) from a KrF excimer laser ($\lambda = 248 \text{ nm}$, 5 Hz repetition) were focused on a stoichiometric polycrystalline Bi_2Se_3 target with a pulse fluence of 3.8 J/cm^2 ; the target-to-substrate distance was 50 mm. The number of laser pulses was 9000 and deposition took 30 min. The average growth rate was approximately 0.46 \AA/pulse . During the deposition of Bi_2Se_3 films, pure (6 N) He gas was introduced into the vacuum chamber, which was evacuated to a base pressure of $4 \times 10^{-4} \text{ Pa}$ and maintained at a constant pressure, using a differential evacuation system. An approximately 500-nm-thick SiO_2 layer was deposited on the Si substrate using thermal evaporation to prevent any effect of the substrate on the subsequent electrical and Seebeck measurements.

The orientation and crystallinity of Bi_2Se_3 films were determined using X-ray diffraction (XRD, Bruker D8) with Cu K α radiation ($\lambda = 1.5406 \text{ \AA}$) in $2\theta-\omega$ and rocking-curve (ω -scan) configurations. To collect detailed structural information on the films, digital images from a high-resolution (HR) transmission electron microscope (TEM) (Philips Tecnai F20), operated at 200 kV, were recorded using a Gatan 2k × 2k charged couple device camera. The TEM specimens were prepared using a standard procedure of mechanical thinning and Ar-ion milling. Surface morphology and film thickness were examined using field-emission scanning electron microscopy (SEM, JEOL JSM-6500) through plane-view and cross-sectional images, respectively. Film compositions were also analyzed using an Oxford energy-dispersive X-ray spectroscopy (EDS) equipped with the SEM instrument at an accelerating voltage of 15 kV, a dead time of 22–30%, and a collecting time of 90 s. The atomic percentage of each film was determined by averaging the values measured at a minimum of 5 distinct areas on the film's surface. The in-plane electrical conductivity, carrier concentration, and mobility were measured at room temperature using a Hall system (Bio-Rad HL5500PC) with van der Pauw geometry. Indium balls were used to improve ohmic contact on the films' surface. Conductivity vs. temperature $\sigma(T)$ values were measured using a Physical Property Measurement System (PPMS, Quantum Design) between 2 K and 300 K, applying the standard 4-probe technique and using silver paste for the contacts. The in-plane Seebeck coefficient at room temperature was determined from the slope of the voltage difference vs. the temperature difference curve, based on a static temperature-difference method [19].

3. Results and discussion

3.1. Deposition temperature- and pressure-dependent crystal structure of Bi_2Se_3 films

Fig. 1a shows the XRD patterns of selected Bi_2Se_3 films deposited at distinct T_s (at 6.7 or 40 Pa for the optimal crystallinity of films in group I, 0.7 Pa for group II). The presence of dominant ($0\ 0\ \ell$) family planes (labeled from PDF#33-0214) clearly indicates that the films are highly c-axis oriented along the growth direction. Bi_2Se_3 has a rhombohedral structure with a space group

$D_{3d}^5(R\bar{3}m)$ that can be described by a hexagonal primitive cell with three 5-atomic-layer thick lamellae (called quintuple layers, QLs) of $-(\text{Se}^{(1)}-\text{Bi}-\text{Se}^{(2)}-\text{Bi}-\text{Se}^{(1)})-$, in which the atomic layers are stacked in sequence along the c -axis [20], as shown in Fig. 1b. Neighboring QLs are held together by a van der Waals (VdW) bond of $\text{Se}^{(1)}-\text{Se}^{(1)}$, which is substantially weaker than the ionic-covalent bonds inside QLs such as $\text{Se}^{(1)}-\text{Bi}$ and $\text{Bi}-\text{Se}^{(2)}$ [21,22]. The weak $\text{Se}^{(1)}-\text{Se}^{(1)}$ bond leads to a c -axis-favored crystal orientation that has the lowest surface energy [23] and enables the preferential formation of sheet-like structures [24]. Notably, the layered crystal structure offers poor thermal conductivity along the c -axis [2,3].

The (012) and (024) peaks of pure bismuth (identified by PDF#85-1331) were observed at 27.3° and 56.3°, respectively, for the films deposited at 0.7 Pa, but these peaks were absent when $P \geq 6.7 \text{ Pa}$, indicating Bi segregation (observed as high Bi enrichment in the 0.7-Pa films; Fig. 3). In addition to the dominant ($0\ 0\ \ell$) orientation, the films deposited at 350 °C showed the minor ($1\ 0\ \ell$) orientation of the BiSe phase (PDF #29-0246). The existence of the major Bi_2Se_3 and the minor BiSe phases in films deposited at 350 °C implies near-unity Se/Bi ratios in the films (more specifically, ratios ranging from 1.05 to 1.25; Fig. 3); the structure of these films may possess double, covalently connected layers of bismuth $-(\text{Bi}-\text{Bi})-$ intercalating in VdW gaps between QLs, and alternating with 2 QLs [12,20,25].

The mosaic structure and crystallinity of the films were determined from the full width at half maximum (FWHM) of the ($0\ 0\ 6$) X-ray rocking curve (Fig. 1c). FWHM decreased with increasing T_s , indicating improved crystallinity and better orientation between the crystallites (grains). At any given T_s , the FWHM also depended on P . The optimal deposition pressure (the pressure at which the smallest FWHM was associated with the optimal crystallinity) changed from 6.7 Pa to 40 Pa as T_s was increased from 200–250 °C to 300–350 °C. The effect of strain on FWHM was neglected because the films were up to at least three hundred nanometers thick. Thus, the present FWHM characteristics can be explained by considering the orientation and sizes of the grains. Large grain sizes reduce the probability of misorientation of the grains and therefore diminish FWHM [26]. Here, the average grain size increased from approximately 100 nm to 500 nm when T_s was increased from 200 °C to 350 °C (Fig. 2), leading to a drop in FWHM from approximately 10° to 2.7°. However, the narrowing of FWHM depended strongly on the orientation between crystallites (grains). Since the films deposited at 0.7 and 173 Pa were comparatively disoriented than those at 40 Pa, the FWHMs at 0.7 and 173 Pa were larger than at 40 Pa.

The detailed structure and orientation of the Bi_2Se_3 film deposited at 300 °C and 40 Pa were characterized using an HR-TEM (Fig. 1d). The P1, P2, and P3 regions, separated by the eye-guiding white lines (boundaries), revealed the granular-polycrystalline structure of the films. Moreover, P1 and P2 partly overlapped and the corresponding fast Fourier transform (FFT) of this overlapping region indexed by {003} patterns of [010] zone axis was performed from the dashed-square area (Fig. 1d, inset). The projected periods along the c -axes of both P1 and P2 were 9.60 \AA , corresponding to (003) planes, which was close to the reported value of 9.55 \AA in Ref. [27]. The c -axis angle between P1 and P2 was approximately 20°, which is the misorientation between grains (platelets) that accounts for the large value of FWHM in Fig. 1c.

3.2. Deposition temperature- and pressure-dependent microstructure of Bi_2Se_3 films

Fig. 2 shows the surface and cross-sectional morphology evolution of Bi_2Se_3 films prepared at various T_s in the 200–350 °C range and P in the 0.7–173 Pa range. At low pressure (0.7 Pa), films deposited at 200 °C were smooth and compact (SC), with

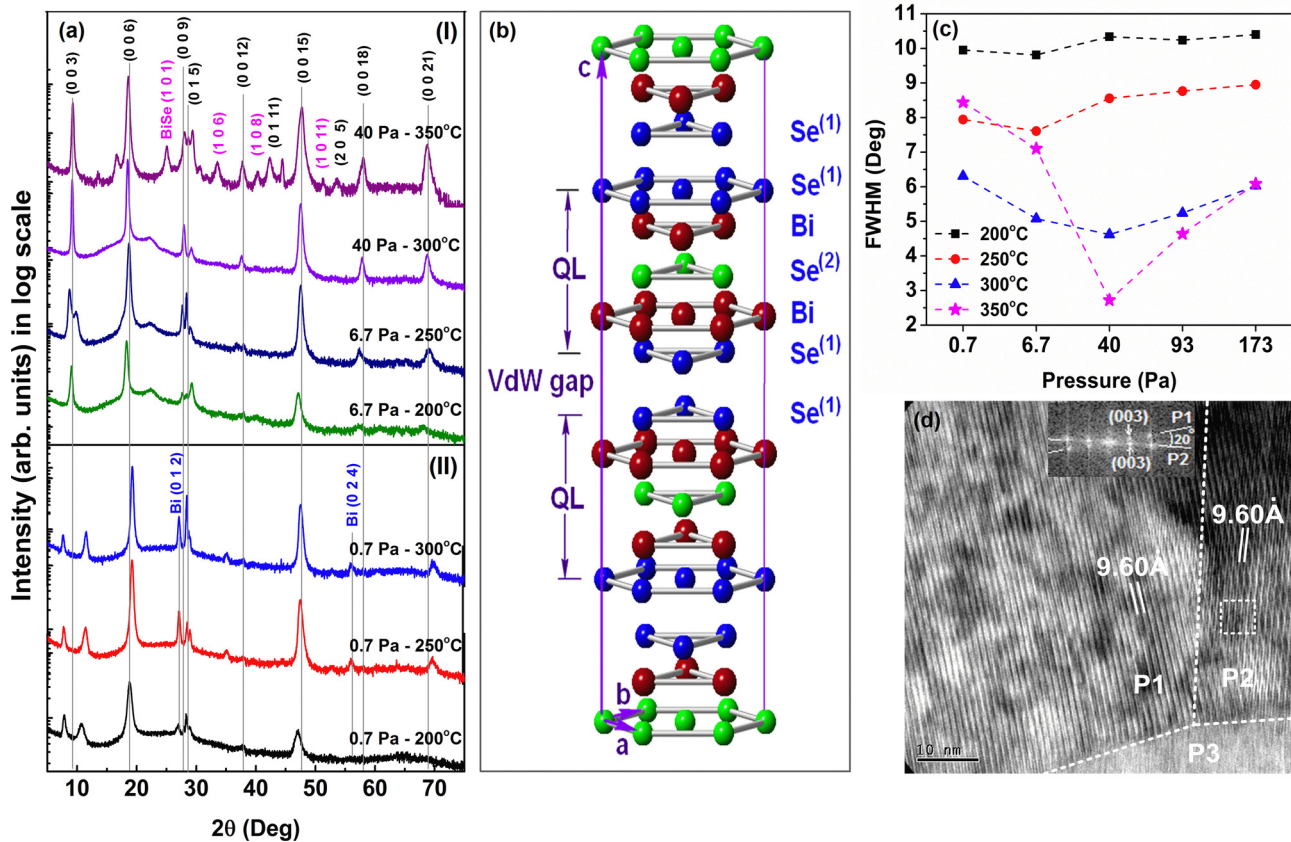


Fig. 1. (a) X-ray diffraction patterns of Bi₂Se₃ films deposited under: (I) 6.7 or 40 Pa, and T_s of 200–350 °C for the best crystallinity films, and (II) 0.7 Pa (the lowest pressure in this study) and T_s of 200, 250, 300 °C. (b) The hexagonal structure of one unit cell of Bi₂Se₃. (c) FWHM vs. pressure of the rocking curve (0 0 6) peaks for Bi₂Se₃ films grown at 200, 250, 300, and 350 °C. (d) An HR-TEM cross-sectional image of an optimized Bi₂Se₃ film deposited at 40 Pa and 300 °C. The inset shows the FFT patterns of the dash square area in the TEM image.

small crystals or droplets on the surface. These structures could further develop into 3-D step-and-terrace triangular-polygonal (TP) and super-layered flake (S-LFs) structures at $T_s = 250$ °C and $T_s \geq 300$ °C, respectively. At intermediate pressures (6.7–93 Pa), the films exhibited rice-like grain (RG) morphology (average grain, approximately 100 nm) at $T_s = 200$ °C and hexagonal platelets (HPs) at $T_s \geq 250$ °C. The average size of HPs increased from 160 nm to 300 nm and 500 nm (approximate values) when T_s was raised from 250 °C to 300 °C and then 350 °C, respectively. At a high pressure (173 Pa), the films showed clear columnar structures, and became less dense because of the presence of nano- and submicrovoids between grains. The columnar structures were formed by the stacking of (1) RGs at $T_s = 200$ and 250 °C; (2) the approximately 25-nm-thick L-HPs grown from bottom to top at $T_s = 300$ °C; and (3) the approximately 38-nm-thick and misoriented L-HPs at $T_s = 350$ °C. We noted that under the same deposition temperatures, films tended to become thicker when P was increased.

The deposition parameters (P , T_s) affect the nucleation and growth of the films. After Bi and Se atoms were deposited on the substrate surface, nucleation (the formation of a single stable nucleus) occurred at supersaturation during the condensation of the adatoms on the substrate. Supersaturation is defined by the ratio between the pressure of the arriving atoms and the equilibrium vapor pressure of the film atoms at T_s [28]. At low T_s (200 °C $\leq T_s \leq 250$ °C), supersaturation was fast, which reduced not only the critical size of the nucleus but also the magnitude of the nucleation energy barrier, and resulted in the growth of numerous, small RGs. However, at high T_s (300 °C $\leq T_s \leq 350$ °C), a reduction in supersaturation rates increased the critical size of the nucleus and the nucleation barrier. Consequently, large nuclei can create

isolate islands on the substrates, which then grow and coalesce because of surface diffusion, grain-boundary migration, and possible re-crystallization, driven by the minimum of the interface and surface energy [28–30]. Thus, HPs with c-axis-preferred orientation or large flakes were formed at high T_s (≥ 300 °C). The formation of HP could be associated with the anisotropic bonding configuration of Bi₂Se₃, leading to that the crystal growth rate along the basal planes is much greater than that along c-axis. Besides, the crystalline facets tend to develop on the low-index planes to minimize the surface energy during growing [22,31]. Thus, the diffusion of atoms at high T_s and the natural layered structure of Bi₂Se₃ results in the assembly of the layered structures for the films deposited at $T_s \geq 300$ °C, which are also observed in the Bi₂Te₃ films deposited at $T_s = 350$ °C and $P = 1.0$ Pa, using radio-frequency magnetron sputtering [14].

At high P , the ablated plume is confined tightly in the forward direction, which makes deposition faster, but the mobility of adatoms is limited by the adsorbed helium [33] to suppress the lateral growth of crystals. In short, increasing P accelerates deposition but slows crystal growth of nuclei. Consequently, columnar structures formed at the highest P (173 Pa) because of faster deposition rather than increased crystal growth. In contrast, the disoriented and large flakes formed at the lowest P of 0.7 Pa because of the high crystal growth rate and the plume expansion effect in which Bi and Se can spread over a large area of the substrate. Notably, the typical open-boundary features of high P can be explained by the shadowing effect, because peaks on the growing surface receive a greater coating flux than valleys do, particularly when the flux has a substantial oblique component, and the adsorbed He atoms likely accumulate in crevices and protect the deposited films from the impact of coating atoms [32,33].

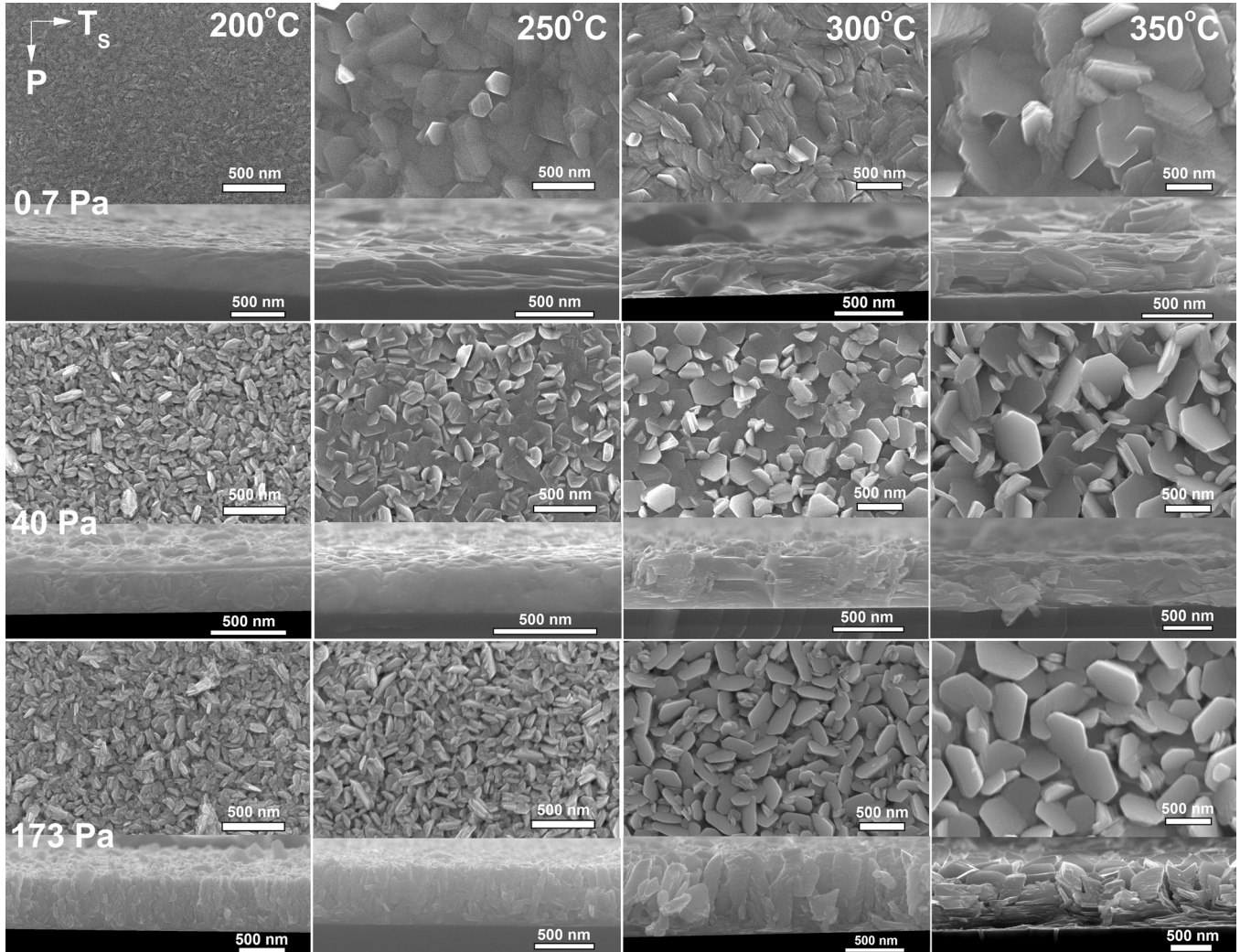


Fig. 2. Cross-section and top view SEM images of the Bi_2Se_3 films deposited at 0.7, 40, and 173 Pa (top-to-bottom), and at 200, 250, 300, 350 °C (left-to-right).

3.3. Deposition temperature- and pressure-dependent compositions of Bi_2Se_3 films

Fig. 3 shows the P - and T_s -dependent compositions of Bi_2Se_3 films. The Se/Bi ratio and the corresponding Se atomic percentage (Se at.%) increased monotonically with increasing P from 0.7 Pa to 93 Pa and then decreased slightly at 173 Pa. In addition, both Se/Bi ratio and Se at.% decreased considerably when T_s was elevated.

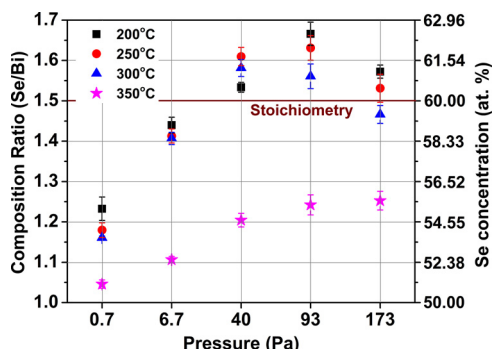


Fig. 3. Background-pressure-dependent compositions, Se/Bi ratio and Se (at.%), of the Bi_2Se_3 films deposited at various T_s ranging from 200 to 350 °C.

Because the vapor pressure of Se is higher than that of Bi ($P_{\text{Se}}/P_{\text{Bi}}$ approximately 10^7 at 300 °C) [15], Se re-evaporates from heated substrates considerably faster than Bi. With the loss of volatile Se atoms from films, Bi atoms segregate on the surface and at grain boundaries [25], as confirmed by the pure Bi peaks in the XRD patterns (**Fig. 1a(II)**) for all highly Bi-enriched (or Se-deficient) films deposited at 0.7 Pa. These results agree with the Bi segregation and XRD patterns reported in Ref. [34]. Noticeably, the remarkable reduction of Se at% at 350 °C is still unclear, probably due to a decrease in Se-sticking coefficient occurred at $T_s > 300$ °C, as such phenomenon has been observed in Bi_2Te_3 film [35].

We next addressed the dependence of film composition on the ambient pressure, P . Bi and Se atoms and ions ejected from the target travel initially at their inherent velocities, and the atoms rebound from the substrate with a certain sputtering yield. At high pressure (≥ 40 Pa), the velocities of Bi and Se atoms equilibrate because of increased collisions with ambient gas atoms, resulting in a spatial confinement of the ablated species. Granular structures are often observed during high- P deposition, suggesting that the vapor species nucleate and grow into particulates before arriving at the substrate under high-pressure [36,37]. The coalescence and growth in later stages assemble these initial particulates and normal nuclei into grains or platelets. Moreover, the high P will reduce the evaporation rates of Bi and Se and shorten the diffusion distance of Bi and Se to keep the rebound atoms close to the substrate. The

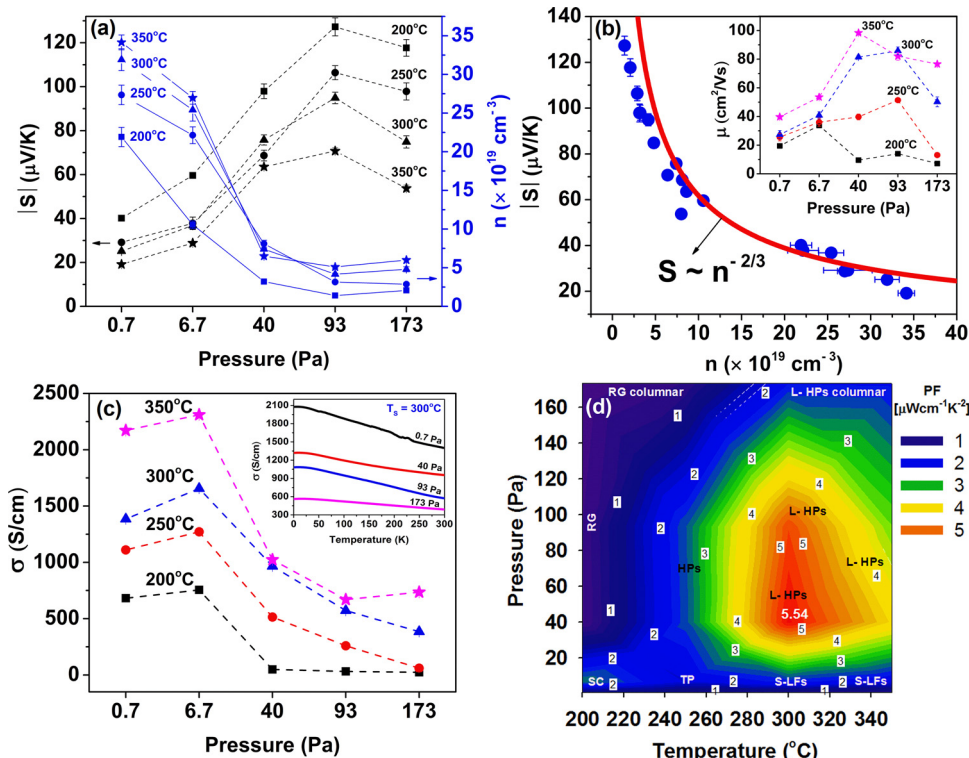


Fig. 4. Pressure-dependent of: (a) carrier concentrations (n) and absolute Seebeck coefficients ($|S|$), (b) The fitting of $|S|$ and n based on $|S| \sim n^{-2/3}$ and the pressure-dependent carrier mobility (μ , inset), (c) pressure-dependent electrical conductivities (σ) of the Bi_2Se_3 films deposited at various T_s from 200 to 350 °C and temperature-dependent conductivities ($\sigma(T)$ in 2–300 K, inset) for the films grown at 300 °C and at various pressures of 0.7, 40, 93, 173 Pa. (d) Contour plot of the film's power factor ($\text{PF} = S^2\sigma$) as a function of background pressure and T_s . The morphology abbreviations: SC, smooth and compact; RG, rice grain; TP, triangular-polygonal; S-LFs, super-layered flakes; L-HPs, layered-hexagonal platelets.

lateral diffusion of the atoms may also be enhanced by the increase in lateral momentum of the rebounded adatoms after several collisions with the ambient gas. Thus, Bi and Se atoms can easily locate their counterparts to form stoichiometric or slightly Se-rich films.

In contrast, at low pressure ($\leq 6.7 \text{ Pa}$), the energetic adatoms generated a larger sputtering yield, which resulted in slower deposition or a thinner film than those under high-pressure growth conditions (Fig. 2). Moreover, the Bi and Se atoms were spread over a large area because the vertical motion of rebounded particles was higher in regions of lower pressure. Therefore, a lower probability of Bi-Se combination and the higher re-evaporation rate of Se than of Bi together yielded Se-deficient films.

3.4. Deposition temperature- and pressure-dependent electrical and TE properties of Bi_2Se_3 films

Fig. 4a shows that the carrier concentration (n) of n-type Bi_2Se_3 films is lowered effectively when P is increased (as also shown by increase of Se concentration in Fig. 3). Carrier concentration, n dropped significantly when P was increased from $\leq 6.7 \text{ Pa}$ to $\geq 40 \text{ Pa}$. This can be attributed to the formation of donor antisite defects, Se_{Bi} (Se occupies Bi site) and Bi_{Se} (Bi occupies Se site) under electron chemical potential $\mu_e < 0.119 \text{ eV}$ [38], which are readily formed in low P than in high P . The minimum value of n is between 1.4 and $3.2 \times 10^{19} \text{ cm}^{-3}$ for films deposited at $T_s \leq 250 \text{ °C}$ and at pressures $\geq 93 \text{ Pa}$. Because the higher vapor pressure of Se renders it more volatile, Bi_2Se_3 is often heavily n-type doped at sites of Se vacancy [16,17]. Se vacancies increased with T_s , and, consequently, led to an increased n , a result that agrees with a previous report on Bi_2Se_3 films grown with $T_s \geq 200 \text{ °C}$ [39].

In contrast to the tendency of n , the absolute value of Seebeck coefficients ($|S|$) monotonically increased with increasing P from 0.7 Pa to 93 Pa, and decreased slightly at 173 Pa. The highest values of $|S|$ were 127.3 ± 4.1 , 106.4 ± 3.2 , 94.9 ± 2.6 , and $70.7 \pm 1.4 \text{ } \mu\text{V/K}$ for $T_s = 200$, 250, 300, and 350 °C, respectively. The value of $|S|$ was slightly lower at higher T_s , which can be attributed to a higher n (likely caused by an increase in the Fermi energy) and an increased grain (crystallite) size at higher T_s . Potential-barrier scattering may further enhance $|S|$ when the grain size becomes smaller, as observed in the PbTe material [40,41].

The Seebeck coefficient depends on the effective number of charge carriers reaching a cold zone. Most thermal carriers are scattered when the doping concentration (n) increased, which leads to a smaller Seebeck coefficient [42]. The relationship between S and n for metals or degenerate semiconductors (i.e., the parabolic band, energy-independent scattering approximation) can be described by Eq. (1) [6,7]:

$$S = \frac{8\pi^2 k_B^2}{3e\hbar^2} m^* T \left(\frac{\pi}{3n} \right)^{2/3} = \frac{A}{n^{2/3}} \quad (1)$$

Fig. 4b shows that $|S|$ can be fitted closely with the $A n^{-2/3}$ relation, using Eq. (1). The fitting coefficient (A) was 70% higher than the expected value in Eq. (1) for $T = 300 \text{ K}$, and $m^* \approx 0.14 m_0$, applied for $n = 7.2 \times 10^{18} \text{ cm}^{-3}$ [43]. The discrepancy arises from the unknown value of m^* and the exclusion of the scattering parameter $R = d \ln \lambda_s / d \ln E_{\text{F}}$ in the fitting, which determines the energy dependence of the carriers' mean free path (λ_s) [7]. To achieve an improved S approximation, as demonstrated for the Bi–Sb–Te nanocrystalline thin film [44], the fitting of our polycrystalline films should include the scattering parameter associated with processes

Table 1

The transport properties (at room temperature) and compositions of some selected Bi_2Se_3 films with different morphologies in this study and the similar Bi_2Te_3 films deposited by PLD [13] and RF sputtering [14].

Morphologies	Deposition conditions		n (10^{19} cm^{-3})	μ (cm^2/Vs)	σ (S cm^{-1})	S ($\mu\text{V/K}$)	PF ($\mu\text{W/cm K}^2$)	Se/Bi at. ratio	Refs.
Rice grains (RG)	200 °C	40 Pa	3.2 ± 0.2	9.6 ± 0.4	49.2 ± 0.2	-98 ± 3.4	0.46 ± 0.03	60.5/39.5	This work
Nanoparticles	300 °C	20 Pa	9.7	14.8	230	-91	1.90	60/40	Chang and Chen [13]
Nanoparticles	300 °C	1.0 Pa	105	8.3	1390	-60	5.0	56.9/43.1	Deng et al. [14]
Layered HPs	300 °C	40 Pa	7.4 ± 0.3	81.4 ± 1.4	963.8 ± 0.4	-75.8 ± 2.3	5.54 ± 0.34	61.3/38.7	This work
Layered structure	350 °C	1.0 Pa	95	12.1	1840	-70	8.8	56.6/43.4	Deng et al. [14]
Layered-HPs columnar	300 °C	173 Pa	4.8 ± 0.3	50.2 ± 3.4	385.5 ± 0.3	-74.9 ± 2.8	2.16 ± 0.16	59.5/39.5	This work
Nanorods	250 °C	0.9 Pa	9.1	2.0	29	-81	0.19	62/38	Chang and Chen [13]
Columnar structure	350 °C	1.0 Pa	246	7.5	2990	-46	6.4	57.2/42.8	Deng et al. [14]

such as acoustic phonon scattering, neutral-ionized impurity scattering, and grain boundary scattering.

The inset in Fig. 4b shows the carrier mobility μ of the Bi_2Se_3 films grown at various pressures and T_s . The mobility ranged from $7.2 \pm 0.2 \text{ cm}^2/\text{Vs}$ to $98.4 \pm 0.5 \text{ cm}^2/\text{Vs}$ and depended on both pressure and T_s . For a specific T_s , maximum μ was reached at different deposition pressures that correlated strongly with optimal crystallinity (Fig. 1c) or a low doping concentration (small n) (Fig. 4a). A larger n (higher doping concentration) coincides in most cases with a higher density of defective scattering centers (ionized impurities), which impedes carrier mobility. The value of μ increased with increasing T_s because defects and grain-boundary scattering from larger grains were diminished. Noticeably, all Bi_2Se_3 films deposited at high pressure (173 Pa) showed lower mobility, which can be attributed to the columnar and voided structures that limit the in-plane transport of carriers in these films.

Fig. 4c shows the electrical conductivity ($\sigma = n\mu e$) of Bi_2Se_3 films deposited at various T_s and P . The value of σ decreased with increasing P because of the substantial lowering of n , whereas σ increased with increasing T_s because the values of both n and μ became higher.

The temperature-dependent, in-plane electrical conductivities ($\sigma(T)$ in 2–300 K) for the Bi_2Se_3 films deposited at 300 °C and at pressures of 0.7, 40, 93, and 173 Pa are shown in the inset of Fig. 4c. Weakly metallic conductivities were observed down to 20 K, which is common in semiconductors with a high carrier concentration and a narrow band gap (approximately 10^{19} cm^{-3} , $E_g \approx 0.3 \text{ eV}$ in this study). Below 20 K, the electrical conductivities became nearly temperature-independent, as expected in the impurity-scattering region. Both PPMS and Hall measurements showed consistent results for conductivities at room temperature, which varied from 385 S cm^{-1} (or $2.60 \text{ m}\Omega \text{ cm}$) to 1400 S cm^{-1} (or $0.71 \text{ m}\Omega \text{ cm}$). Furthermore, the electrical conductivities increased to 564 S cm^{-1} ($1.77 \text{ m}\Omega \text{ cm}$) and 2078 S cm^{-1} ($0.48 \text{ m}\Omega \text{ cm}$) at 10 K, which are comparable to the $0.3\text{--}1.5 \text{ m}\Omega \text{ cm}$ at 10 K reported for Bi_2Se_3 single crystals [17].

Fig. 4d illustrates the contour plot of the PF ($=S^2\sigma$) as a function of P and T_s . The PF of Bi_2Se_3 films increased with increasing T_s from 200 °C to 300 °C because σ became considerably larger but the Seebeck coefficient diminished only slightly. However, for films deposited at 350 °C, PF was lowered primarily because of the reduction in S and not the increase of σ . Furthermore, the PF of Bi_2Se_3 films grown at intermediate pressure was typically higher than the PF of films grown at a low or high pressure, because the growth of films at intermediate pressure yields an optimal value of $S^2\sigma$ ($=5.54 \pm 0.34 \mu\text{W cm}^{-1} \text{ K}^{-2}$ at $T_s = 300 \text{ }^\circ\text{C}$ and $P = 40 \text{ Pa}$) associated with layered-HPs films.

The optimal PF value, $5.54 \mu\text{W cm}^{-1} \text{ K}^{-2}$, obtained in this study is much higher than those reported previously for Bi_2Se_3 with the hexagonal-flake structure ($\text{PF} \approx 0.28 \mu\text{W cm}^{-1} \text{ K}^{-2}$) [9] or for the nanoflake structure ($\text{PF} \approx 0.97 \mu\text{W cm}^{-1} \text{ K}^{-2}$) [10]. Nevertheless,

our result is comparable to the $\text{PF} \approx 5.8 \mu\text{W cm}^{-1} \text{ K}^{-2}$ of Bi_2Se_3 films grown by metal organic-chemical vapor deposition [45], but remains approximately three times lower than the room-temperature PF of Bi_2Se_3 single crystals [17].

Table 1 summarizes the transport properties (at room temperature) and compositions of selected Bi_2Se_3 films of distinct morphologies grown in this study, and compares these properties and compositions with Bi_2Te_3 films of similar morphologies developed by Chang and Chen [13], using PLD and Deng et al. [14], using radio-frequency magnetron sputtering. For a given microstructure, our deposition conditions are typically lower in T_s and higher in P , which helps suppress n . The Bi_2Se_3 films grown in this study and the Bi_2Te_3 films in Ref. [13] share stoichiometric or slightly Se-rich compositions, lower n ($\sim 10^{19}$), and comparable values of S (approximately $75\text{--}98 \mu\text{W cm}^{-1} \text{ K}^{-2}$). The Bi_2Te_3 films in Ref. [14] were deposited at a low P (1 Pa) and a high T_s (300 or 350 °C) and exhibited Te-deficiency, an extremely high n (approximately 10^{21}), and excellent conductivities, but a slightly lower S , which may have generated the high PF values measured for their films.

4. Conclusion

Bi_2Se_3 polycrystalline thin films were deposited on SiO_2/Si (1 1 1) substrates using PLD by controlling the ambient He pressure (P) between 0.7 and 173 Pa and the substrate temperature (T_s) between 200 °C and 350 °C. The Bi_2Se_3 films possessed dense, granular, and columnar structures when deposited at low (0.7 Pa), intermediate (6.7–93 Pa), and high pressures (173 Pa), respectively. The grains swelled considerably with increasing T_s because the surface mobility of adatoms increased when T_s was raised, and grain morphologies evolved from rice-like (average size, approximately 100 nm, $T_s = 200 \text{ }^\circ\text{C}$) to layered structures of hexagonal platelets or flakes (average sizes, approximately 300 and 500 nm at $T_s = 300$ and 350 °C). The in-plane electrical conductivity (σ) decreased with increasing P because of the degradation of crystallinity and the reduction in n . However, σ increased with increasing T_s because of the enhancement in μ , crystallinity, and grain size. Specifically, Bi_2Se_3 films deposited at $P \geq 40 \text{ Pa}$ were stoichiometric or slightly Se rich, which diminished Se vacancies substantially to reduce the carrier concentration (n) to within 1.4×10^{19} to $7.4 \times 10^{19} \text{ cm}^{-3}$ even at a high T_s (up to 300 °C). More crucially, the reduction of n resulted in a substantial increase of $|S|$, following the relation $S \sim n^{-2/3}$ approximately. The films grown at $T_s = 300 \text{ }^\circ\text{C}$ and at $P = 40 \text{ Pa}$, and containing highly c-axis-oriented and layered hexagonal platelets, possessed the highest PF: $5.54 \pm 0.34 \mu\text{W cm}^{-1} \text{ K}^{-2}$, where $S = 75.8 \pm 2.3 \mu\text{V/K}$ and $\sigma = 963.8 \pm 0.4 \text{ S cm}^{-1}$. The enhancement of PF in this study can be attributed to the low n (grown at $P \geq 40 \text{ Pa}$) even at the high- T_s of 300 °C, which yielded a high Seebeck coefficient and excellent electrical conductivity.

Acknowledgements

One of the authors (P.H. Le) is thankful for Prof. K.H. Wu, Prof. Y.-H. Chu, and Prof. J.Y. Juang for the support of using their equipments. Financial support from the National Science Council of the Republic of China (Taiwan) under Contract No.: NSC101-2221-E-009-126-MY2 and NSC 101-2112-M-009-016-MY2 is gratefully acknowledged.

References

- [1] R. Venkatasubramanian, E. Siivola, T. Colpitts, B. O’Quinn, *Nature* 413 (2001) 597–602.
- [2] G.S. Nolas, J. Sharp, H.J. Goldsmid, *Thermoelectrics: Basic Principles and New Materials Developments*, Springer, New York, 2001.
- [3] D.M. Rowe, in: D.M. Rowe (Ed.), *Thermoelectrics Handbook: Macro to Nano*, CRC/Taylor & Francis, Boca Raton, FL, 2006.
- [4] A. Soni, Z. Yanyuan, Y. Ligen, M.K.K. Aik, M.S. Dresselhaus, Q. Xiong, *Nano Lett.* 12 (2012) 1203.
- [5] Y. Sun, H. Cheng, S. Gao, Q. Liu, Z. Sun, C. Xiao, C. Wu, S. Wei, Y. Xie, *J. Am. Chem. Soc.* 134 (2012) 20294–20297.
- [6] G.J. Snyder, E.S. Toberer, *Nat. Mater.* 7 (2008) 105.
- [7] M. Cutler, J.F. Leavy, R.L. Fitzpatrick, *Phys. Rev.* 133 (1964) 1143.
- [8] N.S. Patil, A.M. Sargar, S.R. Mane, P.N. Bhosale, *Appl. Surf. Sci.* 254 (2008) 5261–5265.
- [9] K. Kadel, L. Kumari, W.Z. Li, J.Y. Huang, P.P. Provencio, *Nanoscale Res. Lett.* 6 (2011) 57.
- [10] Z. Sun, S. Liufu, L. Chen, *Dalton Trans.* 39 (2010) 10883.
- [11] A. Bailini, F. Donati, M. Zamboni, V. Russo, M. Passoni, C.S. Casari, A. Li Bassi, C.E. Bottani, *Appl. Surf. Sci.* 254 (2007) 1249–1254.
- [12] A. Li Bassi, A. Bailini, C.S. Casari, F. Donati, A. Mantegazza, M. Passoni, V. Russo, C.E. Bottani, *J. Appl. Phys.* 105 (2009) 124307.
- [13] H.-C. Chang, C.-H. Chen, *CrystEngComm* 13 (2011) 5956.
- [14] Y. Deng, H.-M. Liang, Y. Wang, Z.-W. Zhang, M. Tan, J.-L. Cui, *J. Alloys Compd.* 509 (2011) 5683–5687.
- [15] H. Noro, K. Sato, H. Kagechika, *J. Appl. Phys.* 73 (1993) 1252.
- [16] J. Navrátil, J. Horák, T. Plecháček, S. Kamba, P. Lošťák, J.S. Dyck, W. Chen, C. Uher, *J. Solid State Chem.* 177 (2004) 1704–1712.
- [17] Y. Hor, A. Richardella, P. Roushan, Y. Xia, J. Checkelsky, A. Yazdani, M. Hasan, N. Ong, R. Cava, *Phys. Rev. B* 79 (2009) 195208.
- [19] L.R. Testardi, G.K. McConnell, *Rev. Sci. Instrum.* 32 (1961) 1067.
- [20] H. Lind, S. Lidin, U. Häussermann, *Phys. Rev. B* 72 (2005) 184101.
- [21] G. Wang, L. Endicott, C. Uher, *Sci. Adv. Mater.* 3 (2011) 539–560.
- [22] D. Kong, W. Dang, J.J. Cha, H. Li, S. Meister, H. Peng, Z. Liu, Y. Cui, *Nano Lett.* 10 (2010) 2245.
- [23] C.-N. Liao, H.-D. Shih, P.-W. Su, *J. Electrochem. Soc.* 157 (2010) D605.
- [24] L.D. Alegria, M.D. Schroer, A. Chatterjee, G.R. Poirier, M. Pretko, S.K. Patel, J.R. Petta, *Nano Lett.* 12 (2012) 4711.
- [25] F.-T. Huang, M.-W. Chu, H. Kung, W. Lee, R. Sankar, S.-C. Liou, K. Wu, Y. Kuo, F. Chou, *Phys. Rev. B* 86 (2012) 081104.
- [26] J.E. Brom, Y. Ke, R. Du, D. Won, X. Weng, K. Andre, J.C. Gagnon, S.E. Mohney, Q. Li, K. Chen, X.X. Xi, J.M. Redwing, *Appl. Phys. Lett.* 100 (2012) 162110.
- [27] L. He, Xiu, Y. Wang, A.V. Fedorov, G. Huang, X. Kou, M. Lang, W.P. Beyermann, J. Zou, K.L. Wang, *J. Appl. Phys.* 109 (2011) 103702.
- [28] M. Ohring, *The Materials Science of Thin Films*, Academic Press, San Diego, CA, 1992.
- [29] D.L. Smith, *Thin-Film Deposition: Principles & Practice*, McGraw-Hill, New York, 1995.
- [30] P.B. Barna, M. Adamik, *Thin Solid Films* 317 (1998) 27–33.
- [31] W. Lu, Y. Ding, Y. Chen, Z.L. Wang, J. Fang, *J. Am. Chem. Soc.* 127 (2005) 10112–10116.
- [32] J.A. Thornton, *J. Vac. Sci. Technol.* 11 (1974) 666.
- [33] J.A. Thornton, *J. Vac. Sci. Technol.* 12 (1975) 830.
- [34] G. Koren, T. Kirzhner, E. Lahoud, K. Chashka, A. Kanigel, *Phys. Rev. B* 84 (2011) 224521.
- [35] A. Mzerd, D. Sayah, J.C. Tedenac, A. Boyer, *J. Cryst. Growth* 140 (1994) 365.
- [36] A. Matsunawa, S. Katayama, A. Susuki, T. Ariyasu, *Trans. JWRI* 15 (1986) 61.
- [37] T. Yoshida, S. Takeyama, Y. Yamada, K. Mutoh, *Appl. Phys. Lett.* 68 (1996) 1772.
- [38] L. Xue, P. Zhou, C.X. Zhang, C.Y. He, G.L. Hao, L.Z. Sun, J.X. Zhong, *AIP Adv.* 3 (2013) 052105.
- [39] P. Tabor, C. Keenan, S. Urazhdin, D. Lederman, *Appl. Phys. Lett.* 99 (2011) 013111.
- [40] K. Kishimoto, T. Koyanagi, *J. Appl. Phys.* 92 (2002) 2544.
- [41] J. Martin, L. Wang, L. Chen, G. Nolas, *Phys. Rev. B* 79 (2009) 115311.
- [42] A. Saji, S. Ampili, S.-H. Yang, K.J. Ku, M. Elizabeth, *J. Phys. Condens. Matter* 17 (2005) 2873–2888.
- [43] Z. Wang, T. Lin, P. Wei, X. Liu, R. Dumas, K. Liu, J. Shi, *Appl. Phys. Lett.* 97 (2010) 042112.
- [44] C.-N. Liao, X.-W. Su, K.-M. Liou, H.-S. Chu, *Thin Solid Films* 519 (2011) 4394–4399.
- [45] A. Al Bayaz, A. Giani, M.C. Artaud, A. Foucaran, F.P. Delannoy, A. Boyer, *J. Cryst. Growth* 241 (2002) 463–470.